Journal of Alloys and Compounds 509 (2011) 7508–7514

Contents lists available at ScienceDirect

Journal of Alloys and Compounds

journal homepage: www.elsevier.com/locate/jallcom

Structural, compositional and electrical properties of co-precipitated zinc stannate

A.R. Babar[a], S.B. Kumbhar[a], S.S. Shinde[a], A.V. Moholkar[a], J.H. Kim[b], K.Y. Rajpure[a,*]

[a] *Electrochemical Materials Laboratory, Department of Physics, Shivaji University, Kolhapur 416004, India*
[b] *Department of Materials Science and Engineering, Chonnam National University, 300 Yongbong-Dong, Buk-Gu, Gwangju 500-757, South Korea*

ARTICLE INFO

Article history:
Received 1 April 2011
Received in revised form 16 April 2011
Accepted 19 April 2011
Available online 27 April 2011

Keywords:
Chemical co-precipitation
Zinc stannate
Structural
Electrical properties
Impedance

ABSTRACT

Zinc stannate (Zn_2SnO_4) powders were synthesized by chemical co-precipitation method using stannic chloride pentahydrate ($SnCl_4 \cdot 5H_2O$) and zinc acetate ($Zn(CH_3COO)_3 \cdot 4H_2O$) as precursors in aqueous medium. The influence of sintering temperatures on the structural, compositional, dielectric, electrical and impedance properties has been studied. X-ray diffraction study reveals that samples sintered at 400–1200 °C show combined phases viz. ZnO, SnO_2, Zn_2SnO_4. The observed binding energies of Sn $3d_{5/2}$, Zn $2p_{3/2}$ and O 1s reveal that Sn and Zn are present in oxidized state (Sn–O–Zn). We studied interparticle interactions like grains, grain boundary effects using complex impedance spectroscopy.

1. Introduction

Zinc stannate (Zn_2SnO_4) is an n-type semiconducting material with wide band gap energy of 3.6 eV [1] belonging to the group of “4–2” cubic oxide spinels (“4–2” denotes the combination of valence cations) with general formula AB_2O_4. Bulk zinc-stannate is stable in the inverse spinel structure [2] with a face-centered cubic (fcc) unit cell. Thus, Zn^{2+} (B) ions occupy tetrahedral voids and Zn^{2+} (B) and Sn^{4+} (A) ions randomly occupies octahedral voids. For spinel structures, there is $Z = 8$ formula units per cubic cell and each consist of 32 anions and 24 cations making a total of 56 atoms [3]. The two different types of cations occupying octahedral sites in inverse spinels are either ordered or disordered [4]. Spinel structures can also accommodate large deviations from stoichiometry. High point defect concentrations, especially cation vacancies are present in non-stoichiometric spinels. Both cation disorder and stoichiometry have an influence on properties and they can also influence on each other. Zn_2SnO_4 has a wide range of applications including the transparent electrode [5], anode including Li-ion batteries [6], photocatalyst [7], and gas sensor [8]. However, the coexistence of SnO_2 and Zn_2SnO_4 would be found easily, even at a relatively lower reaction temperature or the lower reaction rate [9–11]. It could be caused by the easy evaporation of partial ZnO [12]. Several processing routes such as solid state calcinations [13], spray pyrolysis [12], hydrothermal method [14] and a mechano-chemical grinding method [15] have been employed to synthesize zinc stannate particles. Cun et al. [16] reported the synthesis of nano-sized Zn_2SnO_4 material using the coprecipitation method with $SnCl_4$ and $ZnSO_4$ in 1:2 molar proportion. The synthetic conditions and the calcination behavior of nano-sized Zn_2SnO_4 materials have been discussed. Fang et al. [17] had studied synthesis and characterization of Zn_2SnO_4 particles by hydrothermal growth technique. The influence of reaction conditions such as concentrations of mineralizer, reaction temperatures and reaction times on the formation of Zn_2SnO_4 was described. Stambolova et al. [18] atomized aqueous solutions of $SnCl_4$ and $Zn(NO_3)_2$ in air at temperatures of 450–480 °C to synthesize the Zn_2SnO_4 powders, which were subsequently subjected to thermal treatment at 1000 °C for 8–10 h. Belliard et al. [6] used Zn_2SnO_4 prepared by mixing stoichiometric amounts of SnO_2 and ZnO and ball milling for 12 h and then calcining at 1000 °C for 48 h. On the other hand, comparing with the Zn_2SnO_4 films, the synthesis and physical properties of Zn_2SnO_4 nanoparticles are more useful due to its high dielectric constant and co-existence of various phases, Zn_2SnO_4 nanopowders may be applied in electronic devices and used as perfect building blocks of assembling active and integrated nanosystems.

In the present investigation, we have made an attempt to prepare well crystallized Zn_2SnO_4 samples by simple and economical co-precipitation method. The effect of sintering temperature on the phase composition and physicochemical properties of the Zn_2SnO_4 sample has been studied.

---

[*] Corresponding author. Tel.: +91 231 2609435; fax: +91 231 2691533.
E-mail address: rajpure@yahoo.com (K.Y. Rajpure).

0925-8388/$ – see front matter © 2011 Elsevier B.V. All rights reserved.
doi:10.1016/j.jallcom.2011.04.105

2. Experimental

2.1. Preparation of samples

The zinc stannate samples were prepared by a chemical co-precipitation method using AR grade equimolar (0.1 M) stannic chloride pentahydrate ($SnCl_4{\cdot}5H_2O$) and zinc acetate [$(CH_3COO)_2$ $Zn{\cdot}2H_2O$] as precursors in 1:2 composition by volume in solution. The preparation conditions were carefully controlled. Double distilled water was used for solution preparation. Solution pH, considered using the relation between pH and concentrations of both the solutions was adjusted to neutral by adding aqueous ammonia to preserve the hydroxide phases of Zn and Sn. The homogeneous solution was prepared by thoroughly mixing both the solutions. White gelatinous precipitate formed, was filtered using Whatmann filter paper No. 17. The precipitate was washed thoroughly until traces of Cl were removed. It was further dried at ambient temperature and sintered at different temperatures within 400–1000 °C for 6 h in air atmosphere. These compositions were further mixed with polyvinyl alcohol as a binder and pressed into pellets of 10 mm diameter and 2–4 mm thickness using a hydraulic press (∼5 tons for 5 min).

2.2. Characterization of samples

The samples were characterized by X-ray diffractometer (Philips, Model PW-3710) using Cu Kα radiation (λ = 1.5406 Å) for structural analysis especially to verdict the crystalline structure. Fourier Transform Infrared (FTIR) spectra of Zn_2SnO_4 samples were recorded on Perkin Elmer FTIR Spectrophotometer (4000–450 cm^{-1}) with KBr as compressed slices to realize the nature of bonds. For finding the binding energies associated with evolved spectral response and composition analysis, the XPS studies were carried out using the model PHI-5400 type X-ray photoelectron spectroscope with monochromatic Mg Kα (1254 eV) radiation source. All binding energies were determined by calibration and fixing the C 1s line to 285 eV. The deconvolution of the XPS peaks was performed using Lorentzian fitting with identical full width at half maximum (FWHM) after a Shirley background subtraction. The AC parameters such as capacitance (C_p) of the samples was measured in the frequency range 20 Hz to 1 MHz using LCR meter (HP 4284 A) to estimate the dielectric constant (ε') using the relation [19],

$$\varepsilon' = \frac{C_p t}{\varepsilon_0 A} \tag{1}$$

where C_p is the capacitance of the pellet, t the thickness of the pellet, A the area of cross section of the pellet and ε_0 the permittivity of free space (8.854×10^{-12} Fm^{-1}). The AC conductivity (σ_{AC}) of the samples was estimated from the dielectric parameters using the relation [20],

$$\sigma_{AC} = \omega \varepsilon' \varepsilon_0 \; \tan \delta \tag{2}$$

where ω the angular frequency and tan δ is the dissipation factor. Resistivity measurements were carried out by two probe method as a function of temperature from room temperature to 500 °C. Silver paste was used to ensure good ohmic contacts. The impedance parameters namely Z' and Z'' for all the samples are measured at room temperature.

3. Result and discussion

3.1. X-ray diffraction studies

X-ray diffraction patterns of zinc stannate samples sintered at different temperatures are shown in Fig. 1. The samples are polycrystalline and fit well with the spinel cubic, hexagonal and tetragonal crystal structures with preferred characteristic temperatures. The intensity and number of diffraction peaks depend on the amount of corresponding phases. The data was analyzed by making use of JCPDS card nos. 24-1470 (spinel cubic Zn_2SnO_4), 05-0664 (hexagonal ZnO) and 77-0447 (tetragonal SnO_2). Samples sintered within 400–800 °C shows nanocrystalline as well as the polycrystalline mixed phases of Zn_2SnO_4, ZnO and SnO_2. As the sintering temperature increases, the intensity of (3 1 1) plane of Zn_2SnO_4 increases up to 1000 °C and then decreases for higher temperature (1200 °C). Other planes such as (2 2 0), (2 2 2), (4 0 0), (3 3 1), (4 2 2), (5 1 1), (4 4 0), (5 3 1), (6 2 0), (5 3 3), (6 2 2), (4 4 4) and (7 1 1) are also observed for Zn_2SnO_4 phase. Prominence of (1 0 0) and (1 0 1) planes of ZnO is observed up to 800 °C and later on it disappears for higher temperatures. Some weak reflections viz. (1 0 2), (1 1 0), (1 0 3), (1 1 2) and (2 0 1) are also seen for zinc oxide. The intensity of (1 1 0) and (1 0 1) planes of SnO_2 goes on increasing up to 1000 °C and then decreases. However, it is interesting that Zn_2SnO_4 and SnO_2 phases emerge with the increase of calcinations temperature to 1000 °C, which is in good agreement with Chen et al.'s report [21]. It is hard to detect the $ZnSnO_3$ under the present synthetic procedure this may be due to the fact that the only stable phases at high temperature in the ZnO–SnO_2 system are Zn_2SnO_4, ZnO and SnO_2. The coexistence of SnO_2 may be caused by two aspects: (1) the evaporation of a part of ZnO and (2) thermal decomposition of precursor. Stambolova et al. [12] and Hashemi et al. [13] had indicated that the evaporation of part of ZnO was the hurdle for preparing the single phase of Zn_2SnO_4. By tuning sintering temperature, it is possible to persuade amount of particular phase in Sn–O–Zn system, which will be useful for variety of applications such as sensor, Li-ion batteries, and photocatalyst.

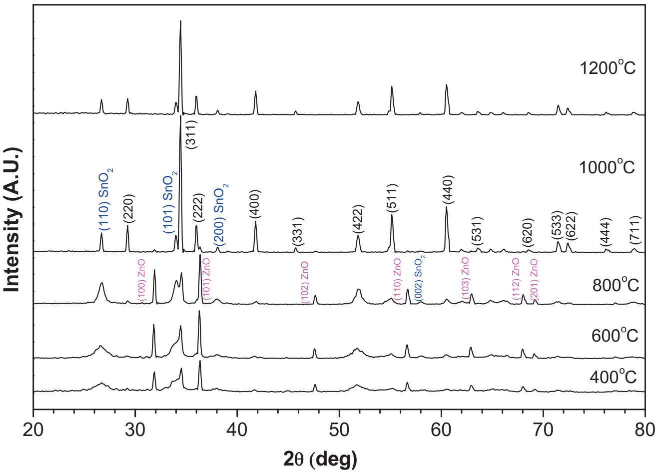

Fig. 1. X-ray diffraction patterns of zinc stannate samples sintered at different temperatures from 400 to 1200 °C.

3.2. Fourier Transform Infrared Spectroscopy (FTIR)

To understand the nature of the species of the Zn_2SnO_4 samples sintered at various temperatures, FTIR spectra of samples was recorded within 450–4000 cm^{-1}. Fig. 2(a)–(d) shows FTIR spectra of samples sintered at various temperatures. The band positions and numbers of absorption peaks are depending on crystalline structure and chemical composition [22]. All IR-bands have been assigned to the absorption peaks of Zn–O, Sn–O, Zn–OH, Sn–OH or OH, C–O bond vibrations. For 400 °C the various absorption bands located at 519, 565, 653, 1016, 1107, 1453, 1641, 2846, 2917, 3438 cm^{-1} are observed. The absorption bands appeared at 519, 501, 499 cm^{-1} for samples sintered at 400–800 °C which are the IR active modes that are theoretically confirmed [23] and it corresponds to wurtzite ZnO. The existence of IR active mode disappears at higher temperature (1000 °C) due to evaporation of ZnO which appears in XRD. From Fig. 2(a)–(d) it is observed that the position of bands centered at 653, 657, 641, and 653 cm^{-1} and around 565 cm^{-1}, for 400 °C, 600 °C, 800 °C and 1000 °C respectively. In all the samples, absorption peaks near 565 and 650 cm^{-1} are corresponding to Sn–O and O–Sn–O vibrations. Tin oxide generally shows the presence of stretching vibrations [24,25]. Also, the other characteristic absorption band has appeared around 1020 cm^{-1} due to both symmetric (ν_1) and antisymmetric stretching (ν_2) vibrations. The peaks of the wave number of 1300–1700 cm^{-1} are the carbonate groups because zinc acetate ($Zn(CH_3COO)_3{\cdot}4H_2O$) has two carboxylic acid groups. This fact indicates that the carbon contained in the precursors forms hydrocarbon and flies out by the effect of sintering. The peaks at 1453, 1462, 1458 cm^{-1} are attributed due to the C–O bands

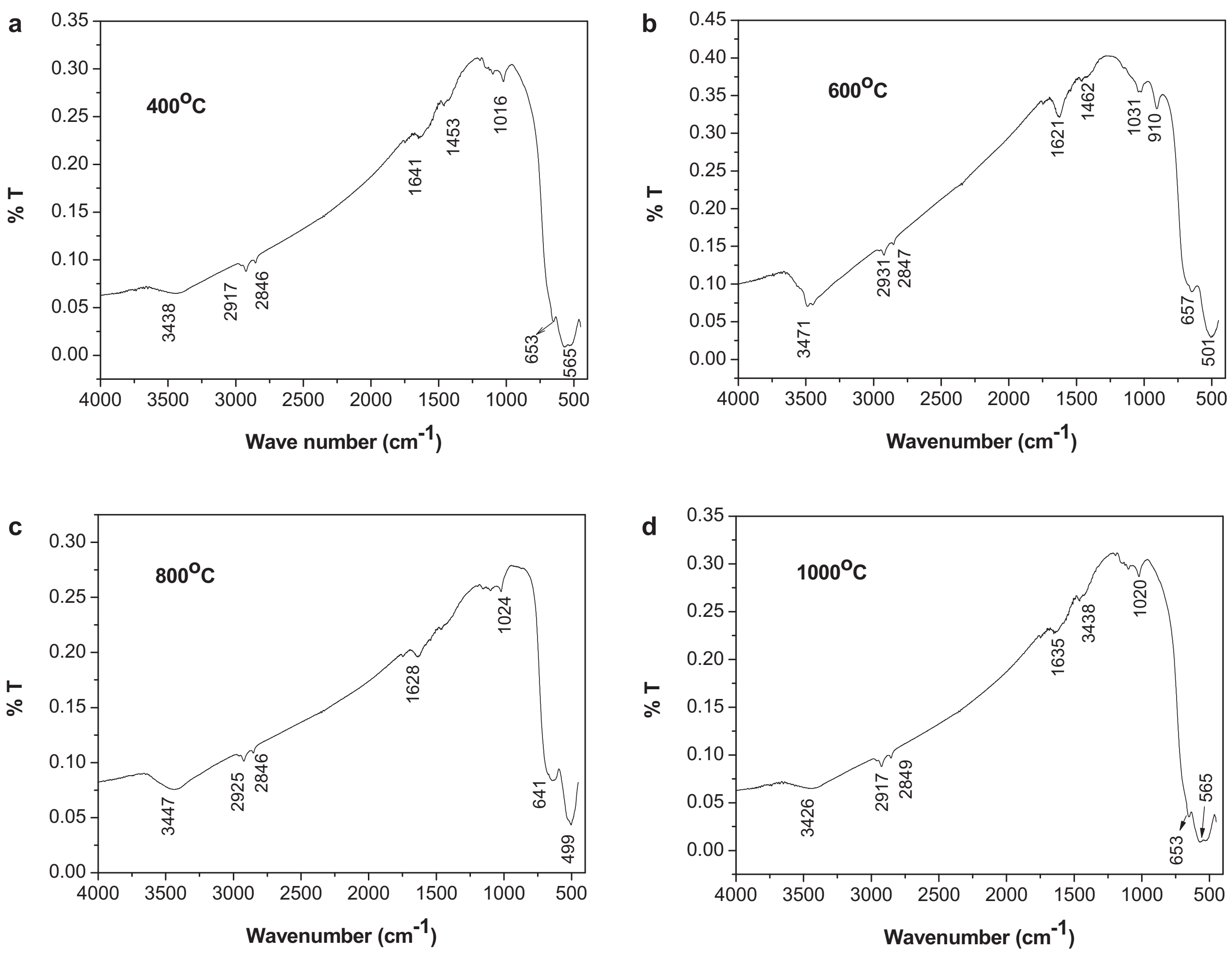

Fig. 2. FTIR spectra of zinc stannate samples sintered at different temperatures: (a) 400 °C, (b) 600 °C, (c) 800 °C, (d) 1000 °C.

[26]. The band at 1640 cm^{-1} is attributed to the O–H deformation mode. The slight shifting of the absorption peak around 1640 cm^{-1} indicates that the formation of the Sn–O and Zn–O groups leads to the decrease of OH groups linked on the surface of the ZnO and SnO_2.

In all the samples the peaks centered at 2917, 2931, 2925 and 2846, 2847, 2849 cm^{-1} are C–H stretching modes in the methyl group. The absorption peaks in the range of 3000–3700 cm^{-1} are assigned to O–H stretching vibration. In the present study, broad bands centered at 3438, 3471, 3447, 3426 cm^{-1} for samples sintered at 400–1000 °C are attributed to the O–H stretching mode. It also contains the mode due to water trapped in the powders.

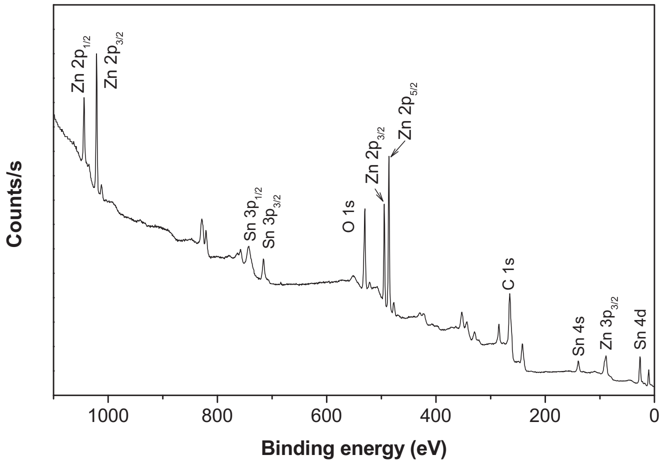

Fig. 3. XPS survey scan spectrum of zinc stannate samples sintered at 1000 °C.

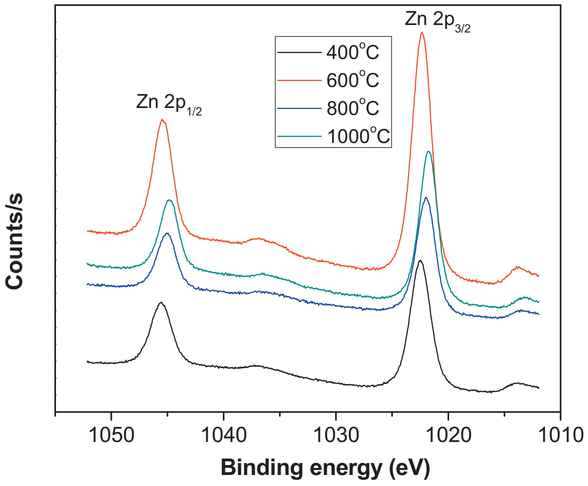

Fig. 4. Sn 3d narrow scan XPS spectra of the zinc stannate samples: (a) 400 °C, (b) 600 °C, (c) 800 °C and (d) 1000 °C.

3.3. X-ray photoelectron spectroscopy

Fig. 3 shows XPS survey scan spectra for the typical Zn_2SnO_4 samples sintered at 1000 °C consisting of Zn, Sn, O and traces of C elements. The presence of C 1s peak in spectra can be attributed to contamination which resulted from the samples being exposed to air before the XPS measurements [27] and due to residual traces of C in the powder. Narrow scan XPS spectra of Zn 2p for all samples are shown in Fig. 4. The spectrum shows well-resolved doublets due to the zinc $2p_{3/2}$ and $2p_{1/2}$ components corresponding to binding energies 1022.49, 1022.32, 1021.98, 1021.75 eV and 1045.58, 1045.44, 1045.03, 1044.81 eV, for samples sintered at 400 °C, 600 °C, 800 °C, and 1000 °C respectively. The binding energy of Zn $2p_{3/2}$ is attributed to the Zn^{2+} bonding state, which agrees well with the previous report [28]. For all the samples, the binding energies of Zn $2p_{3/2}$ is around 1022 eV, the values are higher than that of metallic Zn (1021.1 eV) [29]. It confirms that Zn exists only in the oxidized state. The similar feature had been reported by Mass et al. [30] for doped ZnO thin films. Fig. 5 shows the narrow scan XPS spectra of Sn 3d for all samples. The binding energies of $3d_{5/2}$ and $3d_{3/2}$ are found at 486.65, 486.90, 486.60, 486.47 eV, and, 495.08, 495.32, 495.03, 494.89 eV for samples sintered at 400 °C, 600 °C, 800 °C, 1000 °C respectively. Because of so-called "final-state" effects, the Sn 3d region consisted of a single doublet at binding energies around 495 eV for Sn $3d_{3/2}$ and 487 eV for Sn $3d_{5/2}$, which are in good agreement with the energy reported for SnO_2 [31]. Judging from the positions of the peaks and the symmetry of the Sn 3d line shape, one can reason that tin is only present in the oxidation state Sn^{4+}, assumed since $SnCl_4$ was used as precursor.

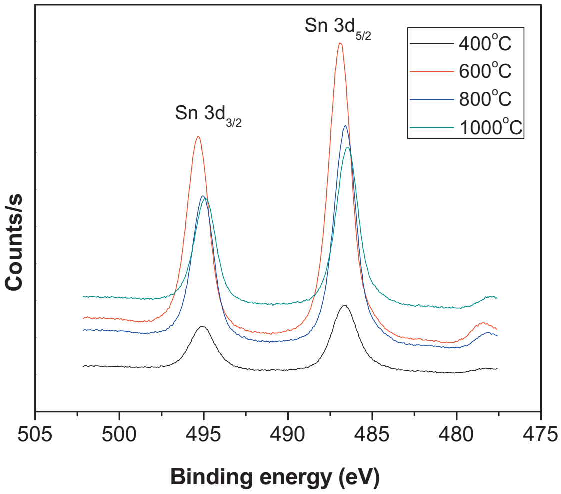

Fig. 5. Zn 2p narrow scan XPS spectra of the zinc stannate samples: (a) 400 °C, (b) 600 °C, (c) 800 °C and (d) 1000 °C.

Similar to Zn, for all the samples, the binding energies of Sn $3d_{5/2}$ is around 487 eV, the values are higher than that of metallic tin (484.65 eV). It confirms that Sn exists only in the oxidized state. As sintering temperature increases the binding energies of Zn and Sn components slightly shift towards the low binding energy due to formation of constituent phases. From the XRD analysis, at 1000 °C, we could see dominance of Zn_2SnO_4 phase with traces of SnO_2. On

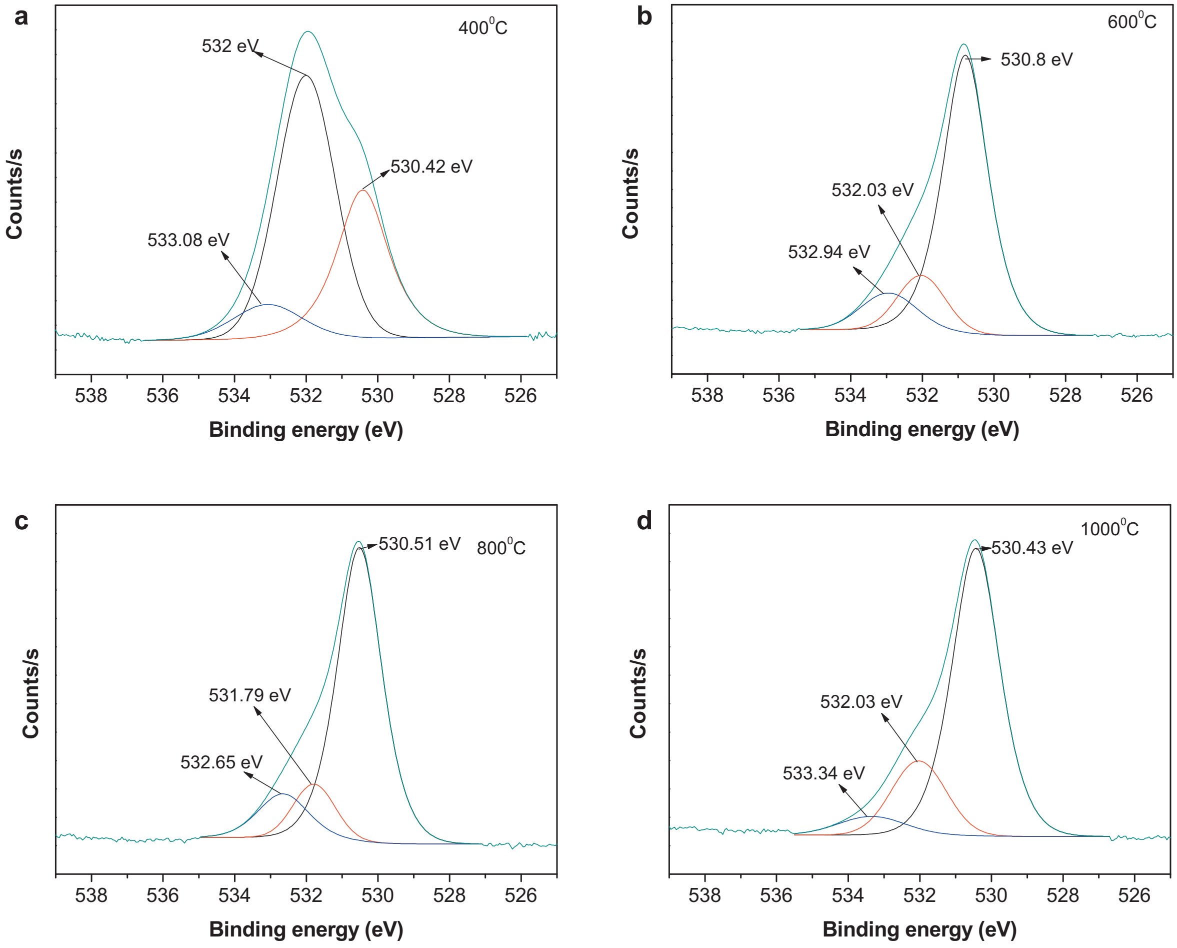

Fig. 6. O 1s narrow scan XPS spectra of the zinc stannate samples sintered in air at various temperatures: (a) 400 °C, (b) 600 °C, (c) 800 °C and (d) 1000 °C.

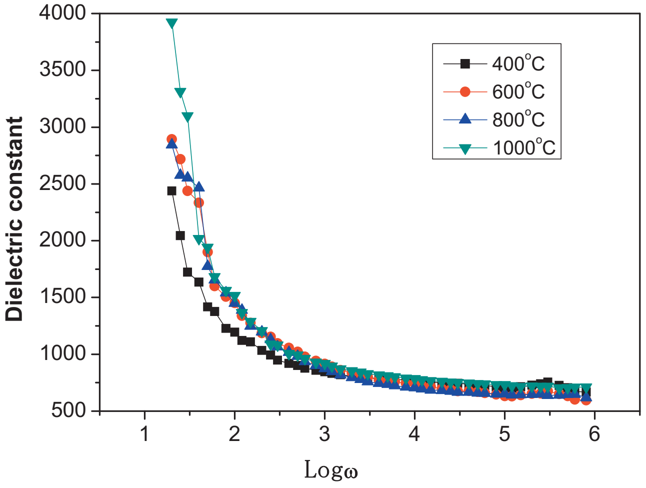

Fig. 7. Variation of room temperature dielectric constant with frequency.

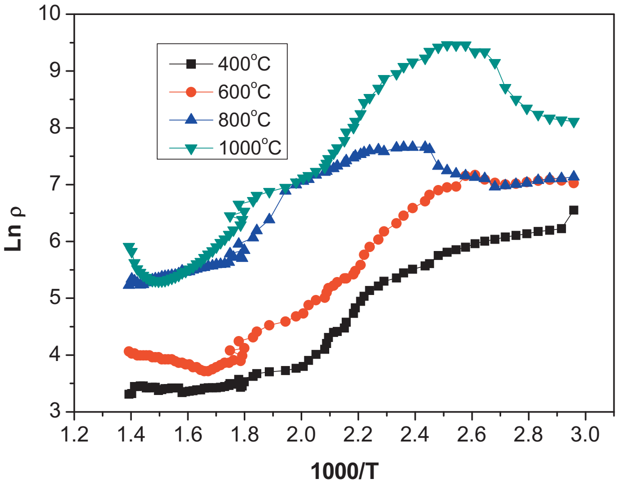

Fig. 9. Variation of dc electrical resistivity with temperature.

the other hand, we could observe the mixture of ZnO, SnO_2 and Zn_2SnO_4 phases at lower sintering temperatures, with less dominance of Zn_2SnO_4 phase. As far as XPS peak positions of Sn 3d and Zn 2p for the sample sintered at 600 °C is concerned, we could see that it is due to Sn and or Zn in SnO_2 and or ZnO respectively. While peak positions of Sn 3d and Zn 2p for the sample sintered at 1000 °C can be assigned to Sn and Zn in lattice of Zn_2SnO_4 as evidenced in Figs. 4 and 5 (change in B.E. for Sn and Zn ~0.5 eV). Therefore at 600 °C, we observe the prominence of Zn and Sn peaks due to dominance of ZnO and SnO_2 phases than Zn_2SnO_4 phase.

Narrow scan XPS spectra of O 1s for samples sintered at 400 °C, 600 °C, 800 °C, 1000 °C are shown in Fig. 6(a)–(d). Gaussian curve fitting illustrates that the O 1s peak has triplet component; such phenomenon is common for oxides containing oxygen in multiple valence states [32]. The binding energies of O 1s triplet are 530.42, 532, 533.08 eV for 400 °C, 530.08, 532.03, 532.94 eV for 600 °C, 530.51, 531.79, 532.65 eV for 800 °C and 530.43, 532.03, 533.34 eV for 1000 °C respectively. The spectrum in Fig. 6(a) shows three components, the major peak is at a binding energy of 532 eV which can be attributed to chemisorbed or dissociated oxygen, or OH type species on the surface of various oxides. Fig. 6(b)–(d) shows the major peak is at a binding energy 530 eV. The major peak at 530 eV is characteristics of oxygen in metal oxide such as Sn–O–Zn, and the other higher binding energy peaks of O 1s in the range 531.7–533 eV has been attributed to chemisorbed or dissociated oxygen, or OH type species on the surface of various oxides. We attribute this presence of O 1s levels to the presence of chemisorbed or dissociated oxygen on the surface of reduced oxide [33]. For the sample sintered at 400 °C the shoulder has observed at 530 eV while for other samples the shoulder is seen around ~532 eV. At 400 °C, relative amount of chemisorbed oxygen, or OH type species is more than lattice oxygen. As sintering temperature increases, the amount of lattice oxygen increases and the amount of chemisorbed oxygen decreases in the samples causing shift of shoulder in O 1s spectra.

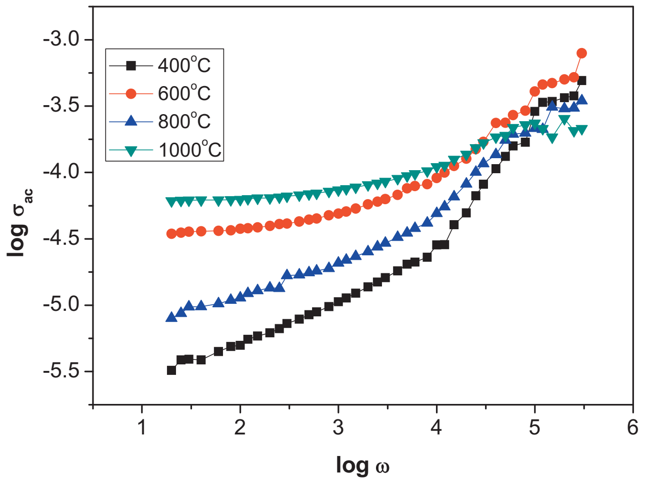

Fig. 8. Variation of AC conductivity with frequency.

3.4. Dielectric properties

The variation of dielectric constant with frequency at room temperature for the samples is shown in Fig. 7. It is clear that dielectric constant (ε_0) decreases abruptly at lower frequencies and remains constant at higher frequencies showing slight dispersion of dielectric constant at lower frequencies. For the samples sintered at 600 °C and 800 °C, there is slight change in crystalline structure and relative amount of Zn_2SnO_4 phase is less than that of SnO_2 and ZnO phases. Therefore there is slight change in dielectric constant for these samples. On the other hand, for the samples sintered at 1000 °C, ZnO phase vanishes and relative amount of SnO_2 is less than that of Zn_2SnO_4, which might be responsible for getting enhanced dielectric constant for this sample. The dielectric constant varies with applied frequency due to charge transport relaxation time. This dielectric dispersion is attributed to Maxwell [34] and Wagner [35] type of interfacial polarization in agreement with Koop's phenomenological theory [36]. Since polarization decreases with increasing frequency and reaches constant values, decrease in dielectric constant with frequency is observed. The large value of dielectric constant is associated with space charge polarization and inhomogeneous dielectric structure. These inhomogeneities are impurities, grain structure and pores.

To confirm the conduction mechanism in these samples, the variation of $\log \sigma_{ac}$ with $\log \omega$ was studied (Fig. 8). The plots are observed to be almost linear indicating that the conductivity increases with increase in frequency. The linearity of the plots confirms small polaron mechanism of conduction. The slight decrease in conductivity is attributed to conduction by mixed polarons. In ionic solids the electrical conductivity is due to migration of ions and the ionic transport depends on angular frequency. Thus, the ac conductivity (σ_{ac}) is proportional to the angular frequency and it

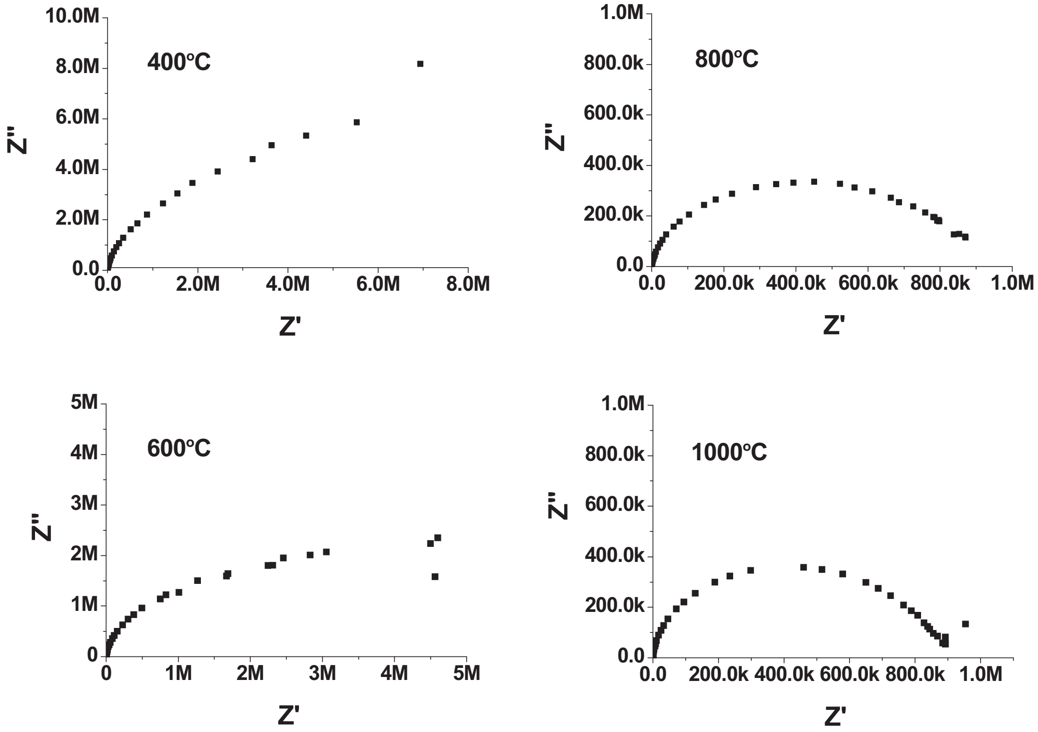

Fig. 10. Nyquist plots for samples sintered at different temperatures.

is confirmed here by linear plots of conductivity with angular frequency [37]. Relatively higher value of dielectric constant and ac conductivity in case of the sample sintered at 1000 °C might be due to dominance of Zn_2SnO_4 phase.

3.5. *Electrical resistivity*

Variation of dc resistivity with temperature is depicted in Fig. 9. The plots show two regions of conductivity. In general, resistivity decreases with increase in temperature suggesting semiconductor behavior of the samples. The first region observed at lower temperatures ($T < 400$ °C) is due to impurities and the second region that occurs at higher temperatures ($T > 400$ °C) is due to polaron hopping [19]. The second region is attributed to the phase transition due to change in activation energy. In the hopping mechanism electrons can 'hop' from one site to another by acquiring the necessary activation energy. Such a thermally activated hopping process is possible at sufficiently high temperatures [38]. The dc resistivity decreases with increasing temperature because with the addition of thermal energy, electron could be set free from O^{2-} ions. When an electron is introduced in the sample it might be associated with cations, which results in an unstable valence state [39]. As the sintering temperature increases, the relative resistivity goes on increasing due to dominance of Zn_2SnO_4 phase. The maximum resistivity observed for the sample calcinated at 1000 °C is perhaps due to the addition of resistivities of constituent phases.

3.6. *Impedance spectroscopy*

The complex impedance formalism helps in determining interparticle interactions like grains, grain boundary effects. The impedance spectrum is usually represented as imaginary component of impedance (Z'') versus real component of impedance (Z'), which is referred as Nyquist plot. The Nyquist plots for all samples recorded at room temperature are shown in Fig. 10. In the present investigation, half semicircle is observed for samples sintered at 400 °C and 600 °C, while for 800 °C and 1000 °C, complete semicircle has observed. As sintering temperature increases, the diameter of the semicircle decreases, indicating a reduction in grain interior resistance. Thus, the total impedance (Z' the real axis intercepts at low frequency side) and imaginary component of complex impedance Z'' of all samples has decreased with increase in sintering temperature. Based on theories of impedance, the occurrence of linear behavior at 400 °C and 600 °C is associated with amount of OH type species on the surface of oxides which are confirmed from XPS studies. As the sintering temperature increases the imaginary part of impedance decreases with real part. The intercept of semicircle with real axis (Z') at low frequency represents the sum of resistances of grains and grain boundaries, while the intercept at high frequency represents the resistance of the grains only. Grain boundary resistance decreases with rise in sintering temperature. This has assisted in lowering the barrier to the motion of charge carriers causing increased electrical transport [40].

4. Conclusions

The zinc stannate samples were prepared by chemical co-precipitation method. The ZnO and SnO_2 phases have emerged at lower calcining temperatures (<800 °C) and a mixed phase containing hexagonal ZnO, tetragonal SnO_2 and spinel cubic Zn_2SnO_4 is formed at higher temperature (1000 °C). The nature of species of various absorption bonds viz. Zn–O, Sn–O, Zn–OH, Sn–OH or OH, C–O involved in sintered Zn_2SnO_4 samples has been studied using FTIR technique. Peaks and symmetry of the Zn $2p_{3/2}$ and Sn $3d_{5/2}$ lines confirm the presence of Zn^{2+} and Sn^{4+} oxidation states. The major peak of O 1s at 530 eV is characteristics of oxygen in metal oxide such as Sn–O–Zn. The dielectric behavior shows the electronic polarizability at higher frequencies due to space charge polarization. AC conductivity increases with increase in the frequency due to hopping mechanism of conduction. The impedance measurement concludes conduction due to grain boundaries.

Acknowledgements

A.R. Babar is highly grateful to University Grants Commission, New Delhi for its support through UGC meritorious fellowship. The authors are thankful to DRDO New Delhi for financial support through Project No. ERIP/ER/0503504/M/01/1007.

References

[1] L. Wang, X. Zhang1, X. Liao, W. Yang, Nanotechnology 16 (2005) 2928.
[2] S.H. Wei, S.B. Zhang, Phys. Rev. B 63 (2001) 045112.
[3] K.E. Sickafus, J.M. Wills, N.W. Grimes, J. Am. Ceram. Soc. 82 (1999) 3279.
[4] R.L. Millard, R.C. Peterson, B.K. Hunter, Am. Mineral. 80 (1995) 885.
[5] J.H. Ko, I.H. Kim, D. Kim, K.S. Lee, T.S. Lee, B. Cheong, W.M. Kim, Appl. Surf. Sci. 253 (2007) 7398.
[6] F. Belliard, P.A. Connor, J.T.S. Irvine, Solid State Ionics 135 (2000) 163.
[7] Y. Lin, S. Lin, M. Luo, J. Liu, Mater. Lett. 63 (2009) 1169.
[8] J.H. Yu, G.M. Choi, Sensor. Actuat. B 72 (2001) 141.
[9] A.A. Al-Shahrani, S. Abboudy, A.W. Brinkman, J. Phys. D: Appl. Phys. 29 (1996) 2165.
[10] J.H. Yu, G.M. Choi, J. Electrochem. Soc. 148 (6) (2001) G307.
[11] R. Yoshida, Y. Yoshida, I. Yamai, K. Kodaira, T. Matsushita, J. Cryst. Growth 36 (1976) 181.
[12] I. Stambolova, K. Konstantinov, D. Kovacheva, P. Peshev, T. Donchev, J. Solid State Chem. 128 (1997) 305.
[13] T. Hashemi, H.M. Al-Allak, J. Illingsworth, A.W. Brinkman, J. Woods, J. Mater. Sci. Lett. 9 (1990) 776.
[14] X. Fu, X. Wang, J. Long, Z. Ding, T. Yan, G. Zhang, Z. Zhang, H. Lin, X. Fu, J. Solid State Chem. 182 (2009) 517.
[15] N. Nikolic, Z. Marinkovic, T. Sreckovic, J. Mater. Sci. 39 (2004) 5239.
[16] W. Cun, W. Xinming, Z. Jincai, M. Bixian, S. Guoying, P. Pingan, F. Jiamo, J. Mater. Sci. 37 (2002) 2989–2996.
[17] J. Fang, A. Huang, P. Zhu, N. Xu, J. Xie, J. Chi, S. Feng, R. Xu, M. Wu, Mater. Res. Bull. 36 (2001) 1391.
[18] I. Stambolova, A. Toneva, V. Blaskov, D. Radev, Ya. Tsvetanova, S. Vassilev, P. Peshev, J. Alloys Compd. 391 (2005) L1.
[19] V.S. Sawant, S.S. Shinde, R.J. Deokate, C.H. Bhosale, B.K. Chougule, K.Y. Rajpure, Appl. Surf. Sci. 255 (2009) 6675.
[20] A.R. Babar, S.S. Shinde, A.V. Moholkar, K.Y. Rajpure, J. Alloys Compd. 505 (2010) 743.
[21] L.Y. Chen, S.L. Bai, G.J. Zhou, D.Q. Li, A.F. Chen, C.C. Liu, Sensor. Actuat. B: Chem. 134 (2008) 360.
[22] Z. Yang, Z. Ye, Z. Xu, B. Zhao, Physica E 42 (2009) 116.
[23] D. Yuvaraj, K.N. Rao, Vacuum 82 (2008) 1274.
[24] S.J.L. Ribeiro, C.V. Santilli, S.H. Pulcinelli, F.J.P. Fortes, L.F.C. Oliveira, J. Sol–Gel Sci. Technol. 2 (1994) 363.
[25] B. Orel, U.L. Stangar, Z.C. Orel, P. Bukovec, M. Korec, J. Noncryst. Solids 167 (1994) 272.
[26] R. Rhodes, M. Horie, H. Chen, Z. Wang, M.L. Turner, B.R. Saunders, J. Colloid Interf. Sci. 344 (2010) 261.
[27] D. Kim, S. Kim, Surf. Coat. Technol. 176 (2003) 23.
[28] S.S. Shinde, K.Y. Rajpure, J. Alloys Compd. 509 (2011) 4603.
[29] S.S. Lin, J.L. Huang, P. Sajgalik, Surf. Coat. Technol. 190 (2005) 40.
[30] J. Mass, P. Bhattacharya, R.S. Katiyar, Mater. Sci. Eng. B 103 (2003) 9.
[31] J.F. Moulder, W.F. Stickle, P.E. Sobol, K.D. Bomben, Handbook of X-ray Photoelectron Spectroscopy, 1995.
[32] A.R. Babar, S.S. Shinde, A.V. Moholkar, C.H. Bhosale, J.H. Kim, K.Y. Rajpure, J. Alloys Compd. 509 (2011) 3108.
[33] A.R. Babar, S.S. Shinde, A.V. Moholkar, C.H. Bhosale, J.H. Kim, K.Y. Rajpure, J. Alloys Compd. 505 (2010) 416.
[34] J.C. Maxwell, Electricity and Magnetism, Oxford University Press, London, 1993, p. 828.
[35] K.W. Wagner, Ann. Phys. 40 (1993) 818.
[36] C.G. Koop, Phys. Rev. B 83 (1951) 121.
[37] S.S. Shinde, C.H. Bhosale, K.Y. Rajpure, J. Alloys Compd. 509 (2011) 3943.
[38] S. Jeon, S. Park, Microelectron. Eng. 88 (2011) 872.
[39] R. Rai, N.C. Soni, S. Sharma, R.N.P. Choudhary, in: A.P. Tandon (Ed.), Ferroelectrics and Dielectrics, Allied Publishers Pvt. Ltd., New Delhi, 2004, p. 177.
[40] S.S. Shinde, A.V. Moholkar, J.H. Kim, K.Y. Rajpure, Surf. Coat. Technol. 205 (2011) 3567.